Original Papers

phys. stat. sol. (a) **42**, 47 (1977)

Subject classification: 1.4; 10

Institut für Festkörperphysik und Elektronenmikroskopie der Akademie der Wissenschaften der DDR, Halle (Saale)

On the Computer Simulation of the Electron Microscopic Diffraction Contrast of Dislocations in Jog and Dipole Configurations[1])

By

K. Scheerschmidt and J. Heydenreich

The computer simulation technique of electron microscopic diffraction contrast is applied to simple models for the calculation of dislocations in jog and dipole configurations. So-called angular dislocations and semi-infinite dislocation dipoles of infinitesimal width are used to approximate curved dislocations by straight dislocation segments. The computer simulation is carried out by a matrix method using two different step widths for the applied integration procedure.

Die Computersimulation des elektronenmikroskopischen Beugungskontrasts wird auf einfache Modelle zur Berechnung von Versetzungen in „Jog-" und Dipolanordnungen angewendet. Zur Annäherung nichtgeradliniger Versetzungen durch geradlinige Versetzungssegmente werden Winkelversetzungen und halbunendliche, infinitesimal breite Versetzungsdipole verwendet. Die Computersimulation wird mit einem Matrizenverfahren unter Verwendung von zwei verschiedenen Schrittweiten für das angewandte Integrationsverfahren durchgeführt.

1. Introduction

The investigation of the electron diffraction contrast of dislocation configurations frequently requires also an exact characterization of curved dislocations. In this paper the contrast of the connecting region between dislocation segments of different inclination and the contrast of discontinuities in the course of a straight dislocation line, like, e.g., in the case of dislocation jogs, are of special interest [1]. For this the concept of the dislocation jog is used in the general sense of the continuum theory without distinguishing between "jogs" and "kinks" [2]. All calculations are carried out on the assumption of elastically isotropic materials.

Dislocation configurations of the mentioned type are of interest for the detection of special microprocesses of plasticity in crystalline materials. A typical example is the hindering of the dislocation movement by the interaction of slip dislocations with other dislocations (forest dislocations) or with point defects (e.g. impurities) and agglomerates of point defects, respectively. For the visualization of such processes an example is given in Fig. 1 where dislocations in a magnesium oxide (100) monocrystal foil are shown in an electron micrograph. In the outline micrograph a) dislocations with traced-off regions forming dipoles can be seen, which were generated by the interaction of the moving dislocations with impurities. Micrograph b) shows such a configuration in detail. In this case the image contrast of the dipole (see arrow) is nearly extinguished. In c) one sees a relatively large dislocation "jog".

For the simple detection of the localization of the defects it is favourable to work with narrow contrast profiles of the dislocation jogs and dislocation dipoles. This can

[1]) Dedicated to Prof. Dr. M. Hieke, on the occasion of his 70th birthday, also on behalf of Prof. Dr. H. Bethge.

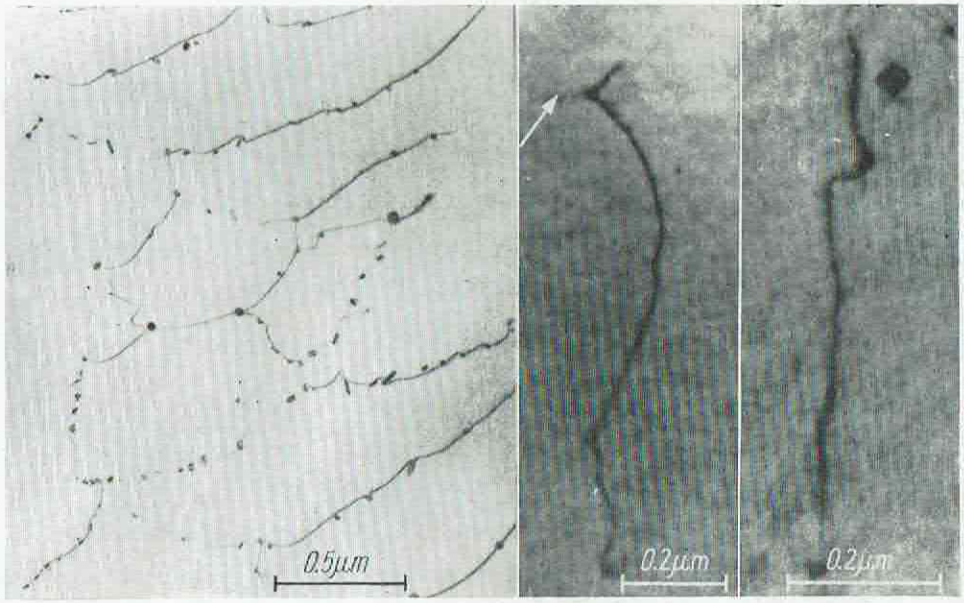

a b c

Fig. 1. Dislocations in a MgO (100) monocrystal foil. a) Survey micrograph, b) dislocation with traced-off dipole, c) dislocation "jog"

be achieved by using the weak-beam technique in the conventional transmission electron microscopy or by the high-order bright-field technique in the high-voltage electron microscopy. For an exact characterization of the type of the defect, however, a computer simulation of the image of the crystal defect and a corresponding comparison with the real electron micrograph are often necessary. In this case it is favourable to apply recording conditions allowing the computer simulation with a relatively low computer expense, which can be achieved by realizing so-called two-beam conditions.

2. Numerical Calculation Methods

Usually the calculation of the computer-simulated electron diffraction contrast due to lattice defects is carried out by means of the well-known Howie-Whelan equations (plane wave formulation) [3] or by means of the Bloch wave formulation of the diffraction equations investigated in detail by Wilkens [4]. The numerical integration of the differential equation system applied in the majority of cases is done by using the Runge-Kutta methods, particularly a procedure developed by Merson (cf. [5, 6]). The presentation of simulated contrast images is realized either by applying the halftone printing technique on the fast line printer of the computer [7], or by controlling the output of display devices [8].

For the computer simulation of dislocations in jog and dipole configurations, being of interest within the scope of this paper, a line printer presentation using overprint and a linear interpolation method are developed which are of course also applicable

determined by interpolation if a suitably chosen criterion is fulfilled. In this way only a small fraction of simulated points — less than 20% — is calculated directly so that by a small computer effort curved defects can be given as a two-dimensional image.

For saving time and to simplify the basic relations of the two-beam case suitable transformation relations are used. For the Bloch wave formulation such a transformation was given by Lepski [9], but also in the case of the plane wave formulation of Howie-Whelan suitable transformation relations can be used to reduce the number of necessary differential equations [10].

In the well-known Howie-Whelan equations the dependence of the amplitudes Φ_0 and Φ_g of the incident and the diffracted electron waves, respectively, on the depth z below the surface of a crystal foil is given by

$$\frac{\mathrm{d}\Phi_0}{\mathrm{d}z} = \frac{i}{2} p \Phi_g \,, \qquad \frac{\mathrm{d}\Phi_g}{\mathrm{d}z} = \frac{i}{2} p \Phi_0 + 2\pi i w_g^{\mathrm{eff}} \Phi_g \,. \tag{1}$$

In this equation all the co-ordinates are reduced using the extinction distance ξ_g. The parameter $p = 2\pi(1 + i\xi_g/\xi_g')$ contains the anomalous absorption coefficient ξ_g'. The effective excitation parameter can be written as $w_g^{\mathrm{eff}} = w_g + \xi_g \beta_g'$, where w_g is the excitation error and β_g', the disturbance function, is the normal derivative of the displacement field component parallel to the diffraction vector: $\beta_g' = \mathrm{d}\boldsymbol{g} \cdot \boldsymbol{u}(\boldsymbol{r})/\mathrm{d}z$.

If $T^{\pm} \exp(\pi i w_g z)$ and $S^{\pm} \exp(\pi i w_g z)$ are solutions of the differential equation system for the perfect crystal:

$$\left.\begin{aligned} T^{\pm}(z) &= \cos(\pi\sigma z) \mp \frac{i w_g}{\sigma} \sin(\pi\sigma z) \,, \\ S^{\pm}(z) &= \frac{i p}{2\pi\sigma} \sin(\pi\sigma z); \qquad \sigma^2 = w_g^2 + \frac{p^2}{4\pi^2} \,, \end{aligned}\right\} \tag{2}$$

then a useful transformation (similar to that of Lepski [9]) can be written as follows:

$$\left.\begin{aligned} r(z) &= \frac{r_2(z)}{r_1(z)} \,, \\ \Phi_{0,g}(z) &= \mathrm{e}^{i\pi w_g z} \left[r_{1,2}(z)\, T^{\pm}(z) + r_{2,1}(z)\, S^{\pm}(z) \right] \,, \end{aligned}\right\} \tag{3}$$

where $r(0) = 0$. Substituting equation (3) into (1) one gets a reduced differential equation system of the Riccati type:

$$r'(z) = 2\pi i \beta_g' (r T^- + S^-)(r S^+ + T^+) \,. \tag{4}$$

The intensities follow from the formulae

$$I_{0,g} = \exp(q) \, |T^{\pm} + r S^{\pm}|^2 \,, \tag{5}$$

where

$$q = -\frac{2\pi \xi_g t}{\xi_0'} + 4\pi \int_0^t \xi_g \beta_g' \, \mathrm{Im}\left[S^* (S^- + r T^-) \right] \mathrm{d}z \tag{6}$$

(ξ_0' normal absorption coefficient).

Another useful time-saving method of integration, which was applied for the computer simulation of the above-mentioned defects, is the matrix multiplication technique given by Thölén [11], within which no special transformations are necessary. For their application in this paper the method is extended to two different step widths Δz_i ($i = 1, 2$) of the slices into which

The amplitudes Φ_0, Φ_g at the lower crystal surface (depth $z = t$) are calculated by the matrix multiplication formulae

$$\begin{pmatrix}\Phi_0(t)\\ \Phi_g(t)\end{pmatrix} = M_n \cdot M_{n-1} \cdot \ldots \cdot M_2 \cdot M_1 \begin{pmatrix}1\\ 0\end{pmatrix}. \tag{7}$$

The matrices $M_k = M_k(\Delta z_j,\ w_g^{\mathrm{eff}}(z_k))$ only depend on an average value of w_g^{eff} within the slice $(z_k,\ z_k + \Delta z_j)$ and the chosen thickness Δz_j of the slice, but do not depend on the depth z_k below the crystal surface.

At the beginning of the calculation of an image 1401 matrices of a step width of Δz_1 in the range $|\xi_g \beta_g'| < 3.5$ and 501 matrizes of a step width of Δz_2 in the range $|\xi_g \beta_g'| < 1.25$ will be calculated and stored in the computer in a suitable way (that means using an increment of $\Delta w = 0.005$ in each case).

If the same notation as above is used, the matrices M_k can be written

$$M_k = \{\exp(\pi i \Delta z_j w_g^{\mathrm{eff}})\} \cdot \begin{pmatrix}T_{\mathrm{eff}}^{+} & S_{\mathrm{eff}}^{+}\\ S_{\mathrm{eff}}^{-} & T_{\mathrm{eff}}^{-}\end{pmatrix}, \tag{8}$$

where the diagonal matrices $\{\exp(\pi i \Delta z_j w_g^{\mathrm{eff}})\}$ only modify the initial values. The functions $T_{\mathrm{eff}}^{\pm}$ and $S_{\mathrm{eff}}^{\pm}$ correspond to the functions $T^{\pm}$ and $S^{\pm}$ (see equation (2)) if w_g is substituted by w_g^{eff} and σ by $\sigma^{\mathrm{eff}} = \left((w_g^{\mathrm{eff}})^2 + p^2/4\pi^2\right)^{1/2}$.

The thicknesses of the slices have to be chosen by computer experiments, because too small Δz_j values lead to errors in the calculation of the $\xi_g \beta_g'$ values. Step widths of $\Delta z_1 = (0.005 \text{ to } 0.01)\ t$ and $\Delta z_2 = (0.05 \text{ to } 0.1)\ t$ were mostly found to be convenient, and the computing time is about half that of the one-step matrix.

After the storage of the matrices M_k the calculation of an image point (x, y), which cannot be interpolated, begins with the large step width Δz_2. The average disturbance function and the difference quotient $\Delta w/\Delta z = [\beta_g'(z_k + \Delta z_j) - \beta_g'(z_k)]/\Delta z_j$ have to be calculated. The quotient $\Delta w/\Delta z_j$ determines the error of selection of the disturbance function within the given slices.

In each case there is a small region around a crystal defect (core region) showing high values of β_g' and causing a considerable error in the determination of the average value of β_g' [10]. But it can be shown that this region around a crystal defect can be calculated in a correct manner if only the jump of the displacement field is considered in the calculation. However, the neglect of the core region in the computer simulation of single crystal defects requires some additional investigations in the case of superposed crystal defects.

3. Models of the Crystal Defects

For the calculation of curved dislocations in the majority of cases it is sufficient to approximate the dislocation line by suitably chosen polygonal dislocation configurations. Using the principle of superposition, which is valid in the linear elasticity theory (distances of more than some Burgers vectors from the core region of the defects), each polygonal dislocation can be composed of straight dislocation segments of finite length. In the case of isotropic materials such straight dislocation segments can be formed using simple dislocation configurations, like, e.g., the infinitesimal dislocation loop given by Kroupa [12] and the semi-infinite dislocation dipole of infinitesimal width [13].

Fig. 3b) and using the mean-value theorem of the integral calculus:

$$u_i(\boldsymbol{r}) = d \int_0^{\infty} f_i\left(x_1, x_2, x_3, \frac{d}{2}, 0, x_3'\right) \mathrm{d}x_3' \,. \tag{9}$$

Here d is the width of the semi-infinite dislocation dipole (see Fig. 2b; $\boldsymbol{d}$ connecting element, $\boldsymbol{t}$ dislocation line) and

$$\mathrm{d}u_i = f_i(\boldsymbol{r}, \boldsymbol{r}')\, \mathrm{d}A \tag{10}$$

is the displacement field of the infinitesimal dislocation loop, using

$$f_i(\boldsymbol{r}, \boldsymbol{r}') = -\frac{k}{\varrho^2}\left[\frac{1-2\nu}{\varrho}(n_i b_k \varrho_k + b_i n_k \varrho_k - \varrho_i b_k n_k) + 3\frac{\varrho_i}{\varrho^3} b_k \varrho_k n_l \varrho_l\right] \tag{11}$$

($\boldsymbol{n} = (n_1, n_2, n_3)$ loop normal, $\boldsymbol{b} = (b_1, b_2, b_3)$ Burgers vector, $\boldsymbol{r} = (x_1, x_2, x_3)$ test point, $\boldsymbol{r}' = (x_1', x_2', x_3')$ integration point, ν = Poisson ratio, $\boldsymbol{\varrho} = \boldsymbol{r} - \boldsymbol{r}'$, $\varrho^2 = \varrho_1^2 + \varrho_2^2 + \varrho_3^2$, $k = 1/8\pi(1-\nu)$).

The gradient normal to the foil surface gives the disturbance function β_g' [10]:

$$\begin{aligned}\beta_g'(\boldsymbol{r}) = kd\,[&(1-2\nu)\,(b_k n_k g_i V_{ij} - g_i n_i b_k V_{kj}) -\\ &- 2(1-\nu)\, g_i b_i n_k V_{kj} + n_l \varrho_l g_i b_k V_{ijk}]\cos(\sphericalangle\, x_j z)\,,\end{aligned} \tag{12}$$

where the abbreviations

$$\left.\begin{aligned} V_i &= \frac{x_i - \delta_{i3} t}{r(r - x_3)}; \qquad \delta_{ij} = \begin{cases}0; & i \neq j\\ 1; & i = j\end{cases}\\ V_{ij} &= \frac{\partial V_i}{\partial x_k} = \frac{\delta_{ik} r^2 - x_i x_k}{r^3 (r - x_3)} - V_i V_k\,,\\ \text{and}\\ V_{ijk} &= \frac{\partial V_{ij}}{\partial x_i} = -\Big[V_i V_j V_k + V_i V_{jk} + V_j V_{ki} + V_k V_{ij} + \frac{x_i}{r^2}(V_j V_k + V_{jk}) +\\ &\quad + \frac{x_j}{r^2}(V_k V_i + V_{ki}) + \frac{x_k}{r^2}(V_i V_j + V_{ij})\Big] \end{aligned}\right\} \tag{13}$$

are used.

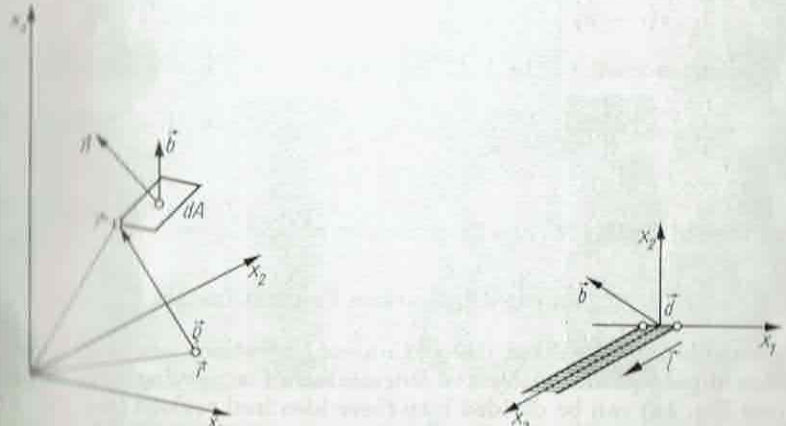

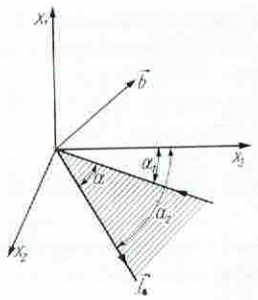

Fig. 3. Geometry of the angular dislocation [14]

Another useful displacement field for the connection of dislocation segments is that of the angular dislocation which was derived by Yoffe [14] from the Burgers formulae (see Fig. 3). Using the correction of Hokanson [15], collecting the various terms, and generalizing to two arbitrary angles α_l ($l = 1, 2$), one obtains the following displacement field:

$$u_i(\boldsymbol{r}) = -\sum_{l}^{1,2} (-1)^l \left[\frac{b_i}{4\pi}\,\Phi^{(l)} + k\mu^{(l)} Q_i^{(l)} + (1-2\nu)\,k\lambda_i^{(l)} \ln\left(r - x_3^{(l)}\right)\right]. \tag{14}$$

The abbreviations are:

$$\left.\begin{aligned}
&\alpha = \alpha_2 - \alpha_1\,, \qquad \alpha_{ij}^{(l)} = \delta_{1i}\delta_{1j} + (\delta_{2i}\delta_{2j} + \delta_{3i3j})\cos\alpha_l + (\delta_{3i}\delta_{2j} - \delta_{2i}\delta_{3j})\sin\alpha_l\,,\\
&x_i^{(l)} = \alpha_{ij}^{(l)} x_j\,, \qquad b_i^{(l)} = \alpha_{ij}^{(l)} b_j\,, \qquad \mu^{(l)} = b_1^{(l)} x_2^{(l)} - b_2^{(l)} x_1^{(l)}\,,\\
&\lambda_i^{(l)} = b_2^{(l)}\alpha_{1i}^{(l)} - b_1^{(l)}\alpha_{2i}^{(l)}\,, \qquad Q_i^{(l)} = \frac{x_i - r\alpha_{3i}^{(l)}}{r\left(r - x_3^{(l)}\right)}\,, \qquad r^2 = x_k x_k\,,\\
&\Phi^{(l)} = \arctan\frac{x_2^{(l)}}{x_1^{(l)}} - \arctan\frac{x_1 r\sin\alpha_l}{x_1 x_1^{(l)}\cos\alpha_l + x_2 x_2^{(l)}}\,.
\end{aligned}\right\} \tag{15}$$

If using the additional abbreviations

$$\Phi_j^{(l)} = \frac{x_1^{(l)}\alpha_{2i}^{(l)} - x_2^{(l)}\alpha_{1i}^{(l)}}{r\left(r - x_3^{(l)}\right)} \quad \text{and} \quad Q_{ij}^{(l)} = \frac{\delta_{ij}r^2 - x_i x_j}{r^3\left(r - x_3^{(l)}\right)} - Q_i^{(l)} Q_j^{(l)}\,, \tag{16}$$

then the gradient normal to the foil surface gives the disturbance function β_g' [10]:

$$\beta_g'(\boldsymbol{r}) = -\sum_{l}^{1,2} (-1)^l \left[\frac{g_i b_i}{4\pi}\,\Phi_j^{(l)} + k g_i a^{(l)} Q_{ij}^{(l)} - k g_i \lambda_j^{(l)} Q_i^{(l)} + (1-2\nu)\,k g_i \lambda_i^{(l)} Q_j^{(l)}\right] \times$$
$$\times \cos\left(\sphericalangle\, x_j z\right). \tag{17}$$

The special case of Yoffe [14] can be chosen by $\alpha_1 = 0$, $\alpha_2 = \alpha$.

4. Computed Diffraction Contrast Images

For the calculations idealized dislocation configurations are used. The image of a dislocation dipole produced by the interaction of a moving dislocation with an obstacle (see Fig. 4a) can be divided into three idealized regions (see Fig. 4b):

Fig. 4. a) Traced-off dislocation dipole and b) simplified representation of different regions

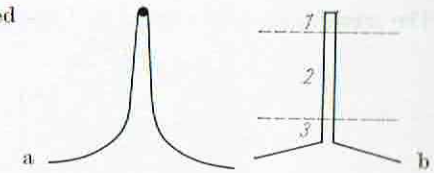

2. the dipole boundary in the region of the obstacle, the image of which can be calculated by taking the displacement field of the semi-infinite dipole;
3. the region where the dipole merges in the original dislocation line.

The latter case can be treated by a suitable combination of two angular dislocations. From the large number of geometrical and imaging parameters only the most important ones for explaining the calculated image are given in each case. Absorption parameters were always chosen in a suitable way.

For regon 1, a frequently treated case, in Fig. 5a comparison of electron micrographs anid matched computer images is shown. These images are related to dislocation dipoles having mainly edge character and lying inclined at an angle of $\gamma = 20°$ in a foil of a thickness of $t = 6\xi_g$. Micrograph 5a shows a dipole, the distance vector $\boldsymbol{d}$ of which is perpendicular to the incident electron beam ($\varphi = 90°$); the distance of the two individual dislocations amounts to $d = 0.1\xi_g$. In Fig. 5b and 5c there are dislocation dipoles with a dipole plane parallel to the incident electron beam ($\varphi = 0°$). The distances are $0.4\xi_g$ in b) and $0.1\xi_g$ in c). The differences in the shapes of the characteristic contrast oscillations can be seen as distinctive marks. The electron micrographs are related to special pre-treated silicon monocrystal foils which nearly fulfil

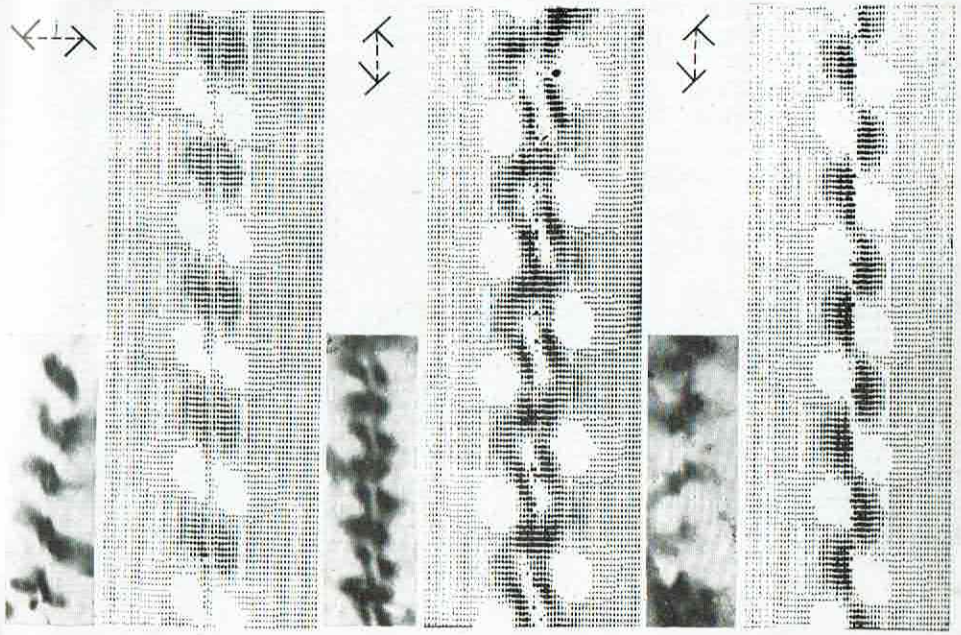

the mentioned geometrical and imaging conditions. The calculation data are:

$$|n| = |\boldsymbol{g} \cdot \boldsymbol{b}| = 1 ,$$

$$p = \frac{1}{3(1-\nu)}\left[1 - \frac{1}{n}(\boldsymbol{g} \cdot \boldsymbol{l})(\boldsymbol{b} \cdot \boldsymbol{l})\right] = 1.05 ,$$

$$|m| = \tfrac{1}{8}\,|\boldsymbol{g} \cdot (\boldsymbol{b} \times \boldsymbol{l})| = 0.12 .$$

For the calculation of the image contrast of region 2 the displacement field of the semi-infinite dipole was used according to equation (12). The computed micrographs for this dislocation configuration are given in Fig. 6. In Fig. 6a the connecting element between the individual inclined dislocation lies at a depth of $1\xi_g$. One sees that the usual dipole contrast is visible up to the place of the connecting element. In this case the parameter is $|n| = 1$, and the connecting element itself is not accentuated by special contrast phenomena. In principle this defect configuration is the same as in Fig. 5a, only the distance of the individual dislocations of the dipole amounts to $0.4\xi_g$ here. In Fig. 6b, for comparison, the region of intersection of a corresponding dipole with the foil surface is shown, the surface relaxation being partially taken into account [16]. One sees that for distinguishing these two cases very fine details must

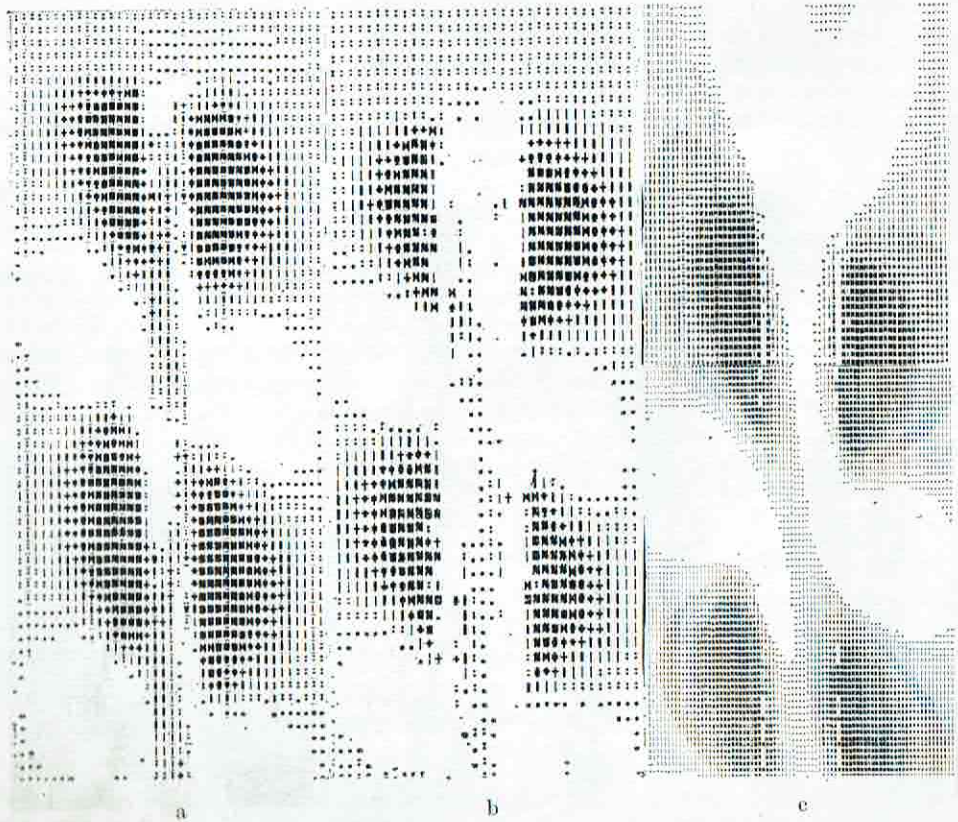

a b c

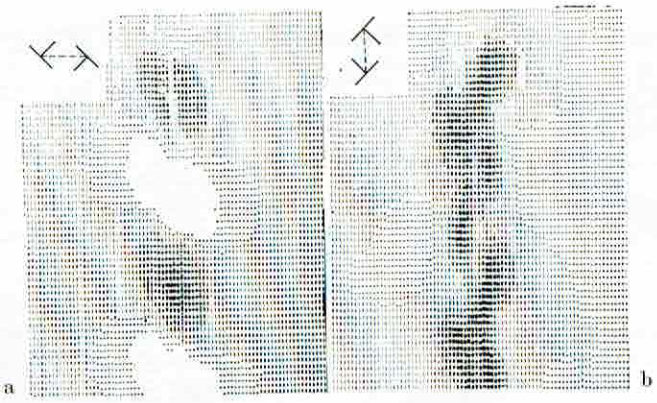

a b

Fig. 7. Semi-infinite dipoles of different positions and different dipole widths d. a) $d = 0.1\xi_g$, b) $d = 0.2\xi_g$

be observed. In addition, the normal case where surface relaxation is not considered is shown in Fig. 6c for comparison. One recognizes a considerable widening of the bright contrast region.

The contrast of a semi-infinite dipole in different positions to the incident beam and with parameters corresponding to Fig. 5a and 5c is represented in Fig. 7. The dipole in Fig. 7a has a distance vector between the individual dislocations which is perpendicular to the incident electron beam, and in Fig. 7b the dipole plane is normal to the surface. While the contrast differences necessary for the characterization of the dipoles are very pronounced, the contrast influences of the connecting regions again give rise only to small modifications of the contrast oscillations in the boundary region.

For the calculation of the region with the traced-off dislocation configuration — region 3 — the displacement field of the angular dislocation according to equation (17) was used. An example of calculations is given in Fig. 8. Here two angular dis-

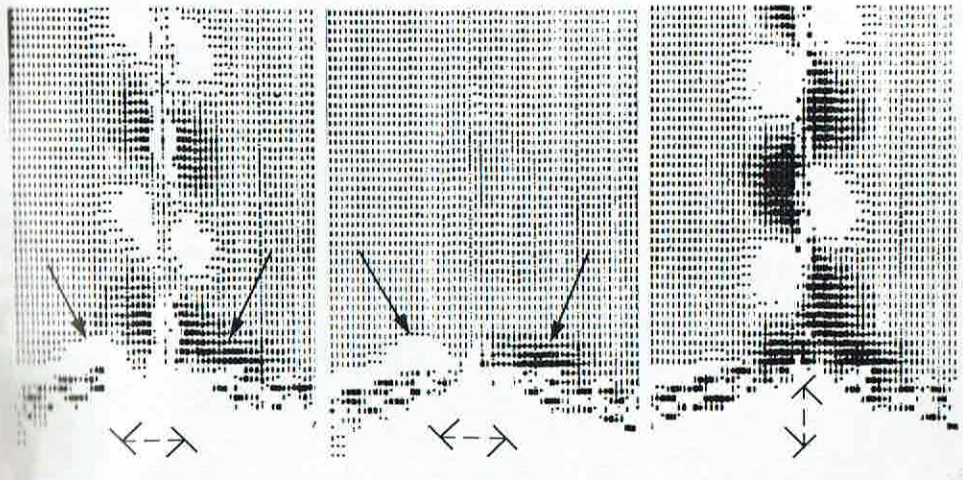

a b c

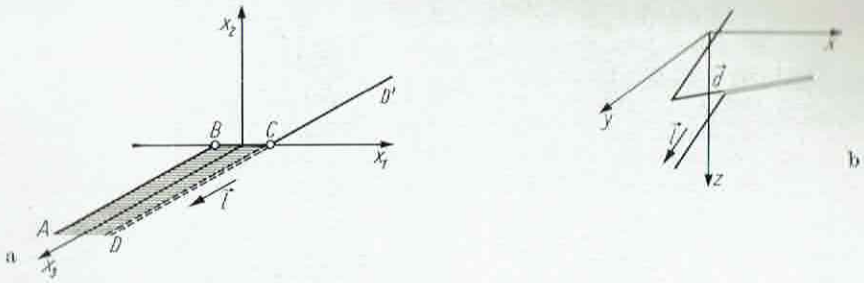

Fig. 9. Principles of superposition for generation of a dislocation jog: a) superposition of a semi-infinite dipole and a straight dislocation line (BC = $\boldsymbol{d}$); b) superposition of two angular dislocations

locations are combined in such a way that an angle of 135° occurs between the two parts of the moving dislocation at which the dipole was formed. The images a) and b) can be related to an assumed dipole plane approximately perpendicular to the incident beam, having a distance of the individual dislocations of $d = 0.1\xi_g$ in a) and $d = 0.01\xi_g$ in b). Remarkable contrast phenomena are the continuous transition of the contrast of the dipole into the contrast of the original dislocation and an asymmetrical contrast behaviour (see arrows) in this region. While in a) with the relatively large distance of the individual dislocations the dipole is clearly visible, in b) there is a contrast loss for this region because of the compensation of the closely neighboured displacement fields. Only an asymmetrical contrast behaviour (see arrow) remains. It will have to be tested whether this phenomenon can be used as a hint for very narrow dislocation dipoles, the contrast of which is extinguished. Fig. 8c is related to a dipole plane lying normal to the surface. A distinction of this position from the preceding one by the pronounced contrast oscillations is possible in an unambiguous manner. The distance d of the individual dislocations of the dipole again amounts to $0.1\xi_g$.

Dislocation "jogs" were calculated in two different ways: On the one hand (see Fig. 9a) by suitable superposition of a Kroupa semi-infinite dipole (ABCD) and a straight individual dislocation line (DCD') with a suitable Burgers vector and sense

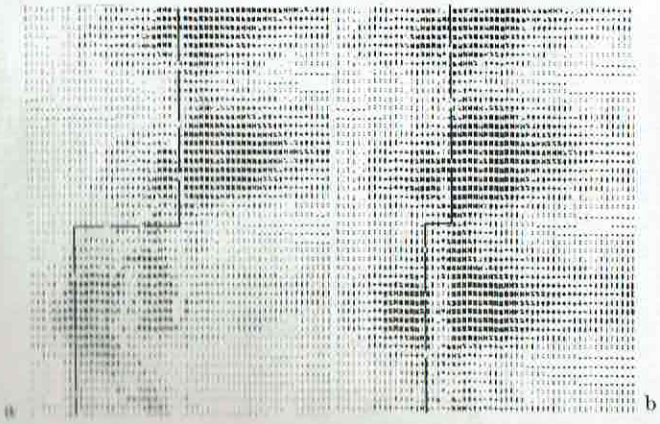

Fig. 10. Dislocation inclined to the foil surface containing a dislocation jog parallel to the surface with different jog sizes d: a) $d = 0.2\xi_g$, b) $d = 0.05\xi_g$. (Note that the dashed lines indicating the

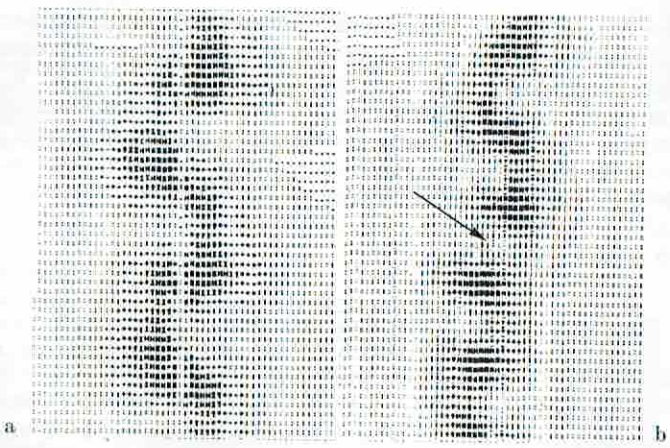

Fig. 11. Mixed dislocation (inclination angle: 45°) a) without dislocation jog; b) with dislocation jog parallel to the surface (depth $t_0 = 2.5\xi_g$, size $d = 0.1\xi_g$)

of direction, so that a regional extinction (DC) of the displacement field configuration results, on the other hand (see Fig. 9b) by a suitable combination of two Yoffe angular dislocations, also with the intention of a sufficient extinction of superposed displacement fields. The computer-simulated images calculated on the basis of these two models showed nearly the same result.

Computed micrographs of "jogs" of different sizes (together with an inscription of their real positions) are shown in Fig. 10. The calculation was done for jog sizes of $0.2\xi_g$ in a) and of $0.05\xi_g$ in b). The jogs are in mixed dislocations inclined at an angle of 36°, the depth of the location of the jogs was $2.5\xi_g$. While in Fig. 10a the jog is directly visible in the micrograph, in Fig. 10b one can only indirectly detect it by analyzing the special contrast oscillations. This situation can be recognized in detail in Fig. 11 where in a) a dislocation without jog and in b) a dislocation with a jog of a height of $0.1\xi_g$ are confronted. The jog itself (see arrow), lying at a depth of $2.5\xi_g$ and obeying the same imaging conditions, manifests itself by a change in the intensities of the contrast oscillations (contrast gap).

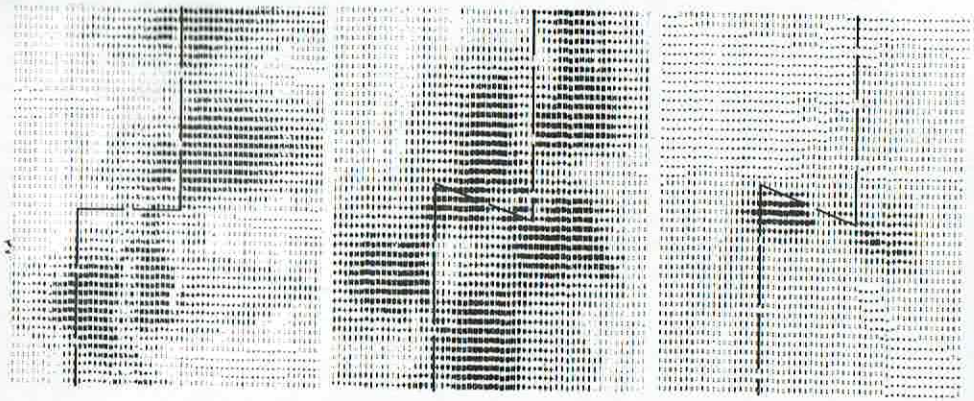

In Fig. 12 the computer-simulated image contrast of a jog lying perpendicular to the direction of incidence (Fig. 12a) is shown in comparison with computed micrographs of jogs lying at an angle of 45° inclined to this direction (Fig. 12 b, c). According to the direction of the chosen Burgers vector there are unsymmetrical image contrasts. Micrograph c) corresponds to the geometry of the defect shown in b). But the diffraction vector for this computed micrograph was chosen in such a way that the condition $\boldsymbol{g} \cdot \boldsymbol{b} = 0$ is fulfilled. The dislocation itself shows no contrast because of fulfilling the additional condition $\boldsymbol{g} \cdot (\boldsymbol{b} \times \boldsymbol{l}) = 0$, and only the jog was visible because $\boldsymbol{g} \cdot (\boldsymbol{b} \times \boldsymbol{l}) + 0$ in this region.

5. Conclusions

Resuming the contrast calculations performed, some connections between defect extent, image contrast, and applicability of the approximations can be concluded:

1. Dislocation jogs in principle show the same dependence of visibility on the defect extent as dislocation dipoles.

2. One can get information by the direct image of jogs and dipoles under normal two-beam conditions (with an adequate expense in computing) down to distances of $0.1\xi_g$. In this region the principle of superposition is valid, but the applicability of the model of the semi-infinite dipole is restricted.

3. For distances between $0.01\xi_g$ and $0.1\xi_g$ conclusions on the character of the corresponding defects are possible only in an indirect way by analyzing the peculiarities of the originating image contrast.

4. The numerical calculations under normal contrast conditions give no contrast for dipoles and jogs if the extent of the defects is smaller than about $0.01\xi_g$. In this region the semi-infinite dipole is a very good approximation, but the principle of superposition is restricted because of the appearance of non-linear effects in elasticity theory.

5. Small jogs, connecting regions between dislocation segments inclined to each other or other small irregularities along otherwise straight dislocation lines, at most influence one depth oscillation of the dislocation contrast in the surroundings of these small deviations.

One of the advantages of the simulation using the concept of the angular dislocation can be seen in the computation of traced-off segments of dislocations in various slip planes: From the beginning the calculation of the angular dislocation takes into consideration the traced-off region of the dislocation, contrary to the method of combining two separately calculated dislocation segments. The application of the described results to the interpretation of more subtile discontinuities in the course of dislocation lines requires the consequent use of the weak-beam technique. The consideration of further diffracted beams, necessary in this situation, leads to a corresponding increase in the computing effort, and to overcome this the development of fast methods for the solution of the many-beam equations of diffraction contrast for an effective work is required. In addition an appropriate extension of the elasticity theory to the actual region of the discontinuities along the dislocation line and the consideration of anisotropic material properties are necessary. Investigations in this direction are still being carried out.

Acknowledgements

References

[1] J. Heydenreich and K. Scheerschmidt, Acta cryst. **A31**, Suppl. 3, 261 (1975).
[2] A. Seeger, in: Hdb. Phys., Vol. VII/2, Springer-Verlag, Berlin 1955 (p. 493).
[3] P. B. Hirsch, A. Howie, R. B. Nicholson, D. W. Pashley, and M. J. Whelan, Electron Microscopy of Thin Crystals, Butterworths, London 1965.
[4] M. Wilkens, phys. stat. sol. **5**, 175 (1964); **6**, 939 (1964).
[5] R. H. Merson, Conf. Proc. Data Processing and Automatic Computing Machines, W. R. E. Salisbury (Australia) 1957 (p. 110).
[6] M. J. Goringe, in: Electron Microscopy in Material Science, Proc. Internat. School Electron Microscopy, Erice (Italy) 1970, Academic Press, New York 1971 (p. 462).
[7] A. K. Head, Austral. J. Phys. **20**, 557 (1967).
[8] D. M. Maher, R. C. Perrin, and R. Bullough, phys. stat. sol. (b) **43**, 707 (1971).
[9] D. Lepski, phys. stat. sol. (a) **23**, 543 (1974); **24**, 99 (1974).
[10] K. Scheerschmidt, Thesis, Halle 1975.
[11] A. R. Thölén, Phil. Mag. **22**, 175 (1970).
[12] F. Kroupa, Czech. J. Phys. **B12**, 191 (1962).
[13] F. Kroupa, phys. stat. sol. **9**, 27 (1965).
[14] E. H. Yoffe, Phil. Mag. **5**, 161 (1960).
[15] J. L. Hokanson, J. appl. Phys. **34**, 2337 (1963).
[16] K. Scheerschmidt, to be published.

(Received February 23, 1977)